Research Square

Preprints are preliminary reports that have not undergone peer review.
They should not be considered conclusive, used to inform clinical practice,
or referenced by the media as validated information.

Coupled Effects of Boundary Corrugation and Hartmann Damping on Nanofluid Convection in Isosceles Triangular Enclosures: A High-Fidelity Thermophysical Analysis

Karim Mehrabi

karim.mehrabi@upm.es

Universidad Politécnica de Madrid

Research Article

Keywords: MHD, Natural convection, Nanofluid, Wavy wall, Triangular enclosure, Hartmann number, Al2O3

Posted Date: July 24th, 2026

DOI: https://doi.org/10.21203/rs.3.rs-10454749/v1

License: This work is licensed under a Creative Commons Attribution 4.0 International License.
Read Full License

Additional Declarations: No competing interests reported.

Version of Record: A version of this preprint was published at Journal of Thermal Analysis and Calorimetry on October 23rd, 2026. See the published version at https://doi.org/10.1007/s10973-026-16494-0.

Coupled Effects of Boundary Corrugation and Hartmann Damping on Nanofluid Convection in Isosceles Triangular Enclosures: A High-Fidelity Thermophysical Analysis

Karim Mehrabi[1*]

[1*]ETSIAE, Universidad Politécnica de Madrid, Plaza Cardenal Cisneros 3, Madrid, 28040, Spain.

Corresponding author(s). E-mail(s): karim.mehrabi@upm.es;

Abstract

This article presents a high-fidelity numerical investigation of magnetohydrodynamic (MHD) buoyancy-driven transport of an $\boldsymbol{Al_2O_3}$-water nanofluid inside a wavy closed isosceles triangular cavity. We employ a customized, non-orthogonal algebraic coordinate transformation mapped onto a custom Discrete Finite Element Method (DFEM) solver to eliminate boundary staircase errors and capture steep localized gradients near the corrugated bottom wall. To address the predictive limits of legacy constant-property models, we implement and contrast two mathematical frameworks: the classical Maxwell-Brinkman formulations and the highly non-linear, temperature-dependent empirical Khanafer-Vafai experimental framework.

The parametric space is systematically analyzed across Rayleigh numbers ($\mathbf{10^3 \leq Ra \leq 10^6}$), Hartmann numbers ($\mathbf{0 \leq Ha \leq 100}$), and nanoparticle volume fractions ($\mathbf{0 \leq \phi \leq 0.06}$). Our computational results reveal that classical homogeneous models consistently underpredict the convective heat transfer enhancement by up to **7.2%** under high-buoyancy states, failing to resolve localized micro-convective thermal paths. Additionally, we characterize the coupled interactions of Lorentz damping and geometric modifications, identifying a critical Hartmann threshold ($\mathbf{Ha \approx 50}$) where electromagnetic forces completely suppress boundary-layer geometric perturbations. These findings establish a mathematically rigorous baseline for active-passive thermal control optimizations in highly restricted physical domains.

Keywords: MHD, Natural convection, Nanofluid, Wavy wall, Triangular enclosure, Hartmann number, $\boldsymbol{Al_2O_3}$

Nomenclature

The following symbols are utilized throughout the governing equations and subsequent parametric analysis:

Roman Symbols

A	Sinusoidal corrugation amplitude	P	Dimensionless pressure
B_0	Magnetic field induction (T)	Pr	Prandtl number
C_p	Specific heat ($\mathrm{J \cdot kg^{-1} \cdot K^{-1}}$)	Ra	Rayleigh number
d_p	Nanoparticle diameter (nm)	T	Temperature (K)
g	Gravitational acceleration ($\mathrm{m \cdot s^{-2}}$)	U, V	Dimensionless velocity components
Ha	Hartmann number	u, v	Dimensional velocity ($\mathrm{m \cdot s^{-1}}$)
k	Thermal conductivity ($\mathrm{W \cdot m^{-1} \cdot K^{-1}}$)	X, Y	Dimensionless coordinates
L	Characteristic scale (m)	x, y	Dimensional coordinates (m)

Greek Symbols

α	Thermal diffusivity ($\mathrm{m^2 \cdot s^{-1}}$)	θ	Dimensionless temperature
β	Expansion coefficient ($\mathrm{K^{-1}}$)	λ	Spatial wavelength
γ	Magnetic field inclination (rad)	μ	Dynamic viscosity ($\mathrm{Pa \cdot s}$)
ϕ	Volume fraction	ρ	Density ($\mathrm{kg \cdot m^{-3}}$)
ψ	Stream function	σ	Electrical conductivity ($\mathrm{S \cdot m^{-1}}$)
ω	Angular frequency		

Subscripts

c	Cold wall boundary	nf	Effective nanofluid
f	Base fluid (water)	s	Solid nanoparticle
h	Hot wavy surface	$*$	Dimensional designation

1 Introduction

Natural convection heat transfer inside enclosed domains constitutes a fundamental pillar of modern thermal engineering, fluid mechanics, and transport phenomena. This sustained interest is fundamentally driven by its ubiquitous role in a wide spectrum of industrial, residential, and high-technology frameworks. Prominent and critical implementations include the design of high-efficiency solar thermal collectors, the optimization of passive building insulation systems, radioactive waste management architectures, nuclear reactor core safety cooling configurations, double-pane window assemblies, and the sophisticated thermal management of advanced aerospace structures [1–4]. In all of these diverse engineering systems, the development, structure, and overall rate of buoyancy-driven fluid circulation serve as the main limiting factors that dictate operational safety limits, net thermodynamic efficiency, and component lifecycle longevity. As contemporary engineering trends inexorably push towards aggressive system miniaturization paired with increasing volumetric power densities—particularly within high-power electronic packaging, avionics, and electric vehicle

(EV) power modules—traditional single-phase heat transfer fluids such as water, ethylene glycol, and synthetic engine oils have rapidly reached their physical cooling limits due to their inherently low molecular thermal conductivities [5–8].

To systematically bypass these classical thermal performance bottlenecks, the paradigm of engineered nanofluids—originally conceptualized by Sheremet and Pop [9]—has emerged as a first high-fidelity strategy to intensively enhance the characteristics of convective and conductive heat transport [10]. Nanofluids are synthesized through the stable long-term suspension of solid nanometer-sized particles (typically ranging between 1 and 100 nm in nominal core diameter) within traditional liquid matrices. The fundamental advantage of these colloidal suspensions stems from the physical reality that solid crystalline phases, whether metallic, metal-oxide, or carbon-based allotropes (such as alumina (Al_2O_3), copper (Cu), or copper oxide (CuO)), possess intrinsic microscopic thermal conductivities that are several orders of magnitude greater than those of their base fluid hosts. During the past few decades, a monumental volume of analytical, experimental, and numerical work has been carried out around the world to rigorously map, predict, and manipulate the effective thermophysical profiles of these multiphase mixtures under various flow states [11–13].

In early classical theoretical and numerical simulations, the standard algebraic formulations developed by Brinkman [14] for effective dynamic viscosity variations and Maxwell [15] for the effective thermal conductivity of spherical-particle suspensions have been widely applied. These legacy models operate under tightly constrained homogeneous mixture assumptions and have been successfully utilized by various contemporary researchers to analyze complex fluid domains. Examples include investigations by Ghasemi and Aminossadati [16] that focus on the behavior of magnetic nanofluids; Hussain et al. [17] for copper-water mixture configurations; Mliki et al. [18] with respect to multi-walled carbon nanotube applications; and Avramenko et al. [19] for a wide variety of oxide-based nanofluid boundary layers.

Nevertheless, extensive contemporary experimental reviews, high-precision laboratory testing, and detailed numerical audits—such as those comprehensively compiled by Tiwari and Das [20], Sheikholeslami and Ganji [21], and Garoosi and Rohani [22]—have consistently revealed severe and non-negligible discrepancies between classical theoretical predictions and real-world laboratory measurements. Crucially, the classical formulations of Brinkman [14] and Maxwell [15] are strictly structured as localized algebraic functions of the static solid volume fraction (ϕ). Consequently, they treat the underlying system as a homogeneous macroscopically static suspension, completely ignoring vital microscale transport dynamics. These include the complex physics of Brownian motion, the formation of localized nanolayers at the liquid-solid molecular interface, the kinetics of cluster aggregation of nanoparticles, and the highly non-linear temperature-dependent sensitivities of the base fluid matrix itself [23–25]. Recent studies have demonstrated that these legacy Maxwell-Brinkman frameworks consistently under-predict thermal conductivity under high buoyancy and steep temperature gradient conditions, necessitating a shift toward more dynamic models [26].

To systematically bridge this predictive gap and increase the fidelity of macroscale computational fluid dynamics (CFD), Khanafer and Vafai [27] developed a comprehensive, physically robust, and experimentally validated thermophysical framework. This advanced formulation synthesizes vast empirical data sets into explicit coupled correlations that directly link effective nanofluid properties to local thermodynamic temperature fields and explicit nanoparticle core diameters (d_p). This ensures an exceptional level of predictive accuracy across broad thermal operating bands where the assumptions of constant-property break down. This physical framework has been further verified, augmented and expanded by complementary formulations of Patel et al. [28] and Ho et al. [29]. These studies universally underscore that realistic heat transfer evaluations must treat the nanofluid medium as a non-linear, temperature-responsive, and morphologically sensitive system rather than a fixed, single-phase Newtonian surrogate.

Parallel to the optimization of the working fluid's internal properties, manipulating the geometric configuration of the enclosing boundaries serves as a highly powerful passive control mechanism for modulating convective fluid streams, localized thermal plumes, and boundary layer thicknesses. Triangular enclosures, and particularly isosceles triangular cavities, have attracted intense academic and industrial research attention due to their direct structural correspondence to attic-shaped residential buildings, industrial warehouses, triangular solar cavity receivers and specialized wedge-shaped electronic heat sinks [30–32]. Early foundational investigations by Khanafer et al. [2], Ghasemi and Aminossadati [33], and Hasan and Saha [34] established that natural convection inside triangular geometries is uniquely constrained by the presence of asymmetric sloping roofs and varying aspect ratios, making the resulting recirculation vortices and buoyant plumes extraordinarily sensitive to minor spatial modifications.

To further regulate these convective structures without the deployment of external power inputs, the implementation of non-flat, wavy, or corrugated boundaries along active heat-exchanging walls has been widely adapted as an optimization strategy [35–37]. Wavy boundaries alter the heat transfer landscape via a dual mechanism: they substantially expand the total effective surface area available for conductive heat transfer into the fluid domain, and introduce localized hydrodynamic perturbations, localized flow detachment zones, and unique secondary reattachment eddies [38, 39]. Detailed parametric studies by several independent research groups have confirmed that carefully adjusting the geometric corrugation amplitude (A) and spatial wavelength (λ) can actively enhance or systematically suppress the global Nusselt number. This outcome strongly depends on whether the core flow field is governed by a conduction-dominated low-Rayleigh (Ra) regime or a highly advection-dominated high-Rayleigh (Ra) regime [40–43].

Although complex boundary modifications provide a reliable passive approach to flow regulation, many advanced industrial applications require a highly responsive, real-time, active control mechanism to tune heat transfer rates on-demand. This crucial capability is effectively provided by the strategic application of an external magnetic field. The discipline of magnetohydrodynamics (MHD) governs the complex, multi-physics coupling between a moving, electrically conducting fluid and an

applied magnetic field induction vector (B_0). As the conducting fluid circulates under the influence of buoyancy forces, its interaction with the magnetic field induces electrical currents, which in turn generate an orthogonal Lorentz force. This force acts in direct opposition to the local fluid velocity vector, acting as a highly controllable, non-invasive electromagnetic brake [44–46]. Recent investigations of magnetohydrodynamic damping highlight that this Lorentz-induced shear stress is a governing factor in stabilizing convective plumes, offering significant control over flow morphology in advanced manufacturing and thermal processing [47].

The use of magnetic fields to control and stabilize thermal convection has found widespread deployment in high-stakes fields such as molten metal purification, semiconductor crystal growth manufacturing, and the cooling blankets of advanced nuclear fusion reactors [48, 49]. In the specific realm of nanofluids, where the baseline electrical conductivity (σ) of the system is fundamentally altered by the suspension of metallic or metal-oxide nanoparticles, the investigations by Selimefendigil and Oztop [50] and Dogonchi et al. [51] have demonstrated that the net intensity of the magnetic field (quantified via the dimensionless Hartmann number, Ha) along with its spatial inclination angle (γ) can be dynamically modulated to completely suppress hydrodynamic instabilities, reshape core streamlines, and optimize multi-phase thermal mixing profiles.

Despite the extensive volume of literature that separately addresses aspects of these individual transport mechanisms, there remains a critical, distinct gap in the existing state-of-the-art on their simultaneous numerical integration. The vast majority of published numerical models either confine their physical scopes to simplified flat-walled cavities, rely on constant-property nanofluid assumptions, or implement classical Maxwell-Brinkman models that fail to track localized temperature dependencies. To the authors' best knowledge, a comprehensive investigation that simultaneously models the fully coupled multi-physics interactions of an inclined magnetic field, complex sinusoidal base wall corrugations, and the temperature-dependent Khanafer-Vafai experimental nanofluid framework inside an isosceles triangular enclosure has not yet been reported in the open literature.

The principal objective of the present study is to fill this research gap by providing a grid-independent high-fidelity numerical analysis utilizing a custom-developed Discrete Finite Element Method (DFEM) compiled and optimized within a high-performance Fortran computing environment. The core focus is directed toward illuminating how variations in the sinusoidal corrugation amplitude (A) and spatial wavelength (λ) interact with a broad spectrum of dimensionless parameters, namely Rayleigh numbers ($10^3 \leq Ra \leq 10^6$), Hartmann numbers ($0 \leq Ha \leq 100$) and solid nanoparticle volume fractions ($0 \leq \phi \leq 0.06$). The comprehensive data sets, flow streamlines, and localized thermal field maps generated from this work are intended to offer practical design guidelines and optimization maps for the engineering of next-generation high-performance compact heat exchangers and thermal management systems.

From a practical standpoint, the symmetric isosceles triangular configuration studied here serves as a direct, simplified analog for thermal transport in attic-shaped spaces, triangular solar cavity receivers, and wedge-shaped electronic heat sinks. In

these systems, managing heat transfer via passive boundary modifications (corrugation amplitude A and frequency λ) and active electromagnetic controls (Hartmann number Ha) is of key interest. This work establishes a high-fidelity numerical framework to analyze these competing active-passive mechanisms under highly realistic, non-linear thermophysical conditions.

2 Governing Equations and Mathematical Formulation

The present study investigates the steady two-dimensional laminar natural convection of an Al_2O_3-water nanofluid within a closed isosceles triangular enclosure under the influence of a uniform horizontal magnetic field. The physical configuration, coordinate allocation metrics, and schematic boundary parameters are presented in Fig. 1. The bottom wall is characterized by a sinusoidal wavy profile and is maintained at a constant high temperature (T_h), while the remaining inclined straight walls are kept at a constant cold temperature (T_c). A uniform external magnetic field of strength B_0 is applied to the system along the horizontal direction. The fluid medium is assumed to be incompressible and Newtonian, implementing the standard Boussinesq approximation to resolve buoyancy-driven density variations.

The spatial profile of the sinusoidal corrugated bottom boundary, which spans horizontally throughout the domain width from $x^* = -L$ to $x^* = L$, is explicitly governed by the following analytical formulation.

$$y^*_{\text{bottom}}(x^*) = A^* \left[\cos\left(\frac{2\pi x^*}{\lambda^*} \right) - 1 \right] \tag{1}$$

where A^* denotes the dimensional amplitude of the surface corrugations, and λ^* signifies the characteristic wavelength.

Displacement currents, induced magnetic field disturbances, viscous dissipation, and Joule heating are assumed to be negligible. Under these constraints, the dimensional governing partial differential equations representing the conservation of mass, momentum, and energy are expressed as follows:

$$\frac{\partial u^*}{\partial x^*} + \frac{\partial v^*}{\partial y^*} = 0 \tag{2}$$

$$u^* \frac{\partial u^*}{\partial x^*} + v^* \frac{\partial u^*}{\partial y^*} = -\frac{1}{\rho_{nf}} \frac{\partial P^*}{\partial x^*} + \frac{\mu_{nf}}{\rho_{nf}} \left(\frac{\partial^2 u^*}{\partial x^{*2}} + \frac{\partial^2 u^*}{\partial y^{*2}} \right) - \frac{\sigma_{nf} B_0^2}{\rho_{nf}} u^* \tag{3}$$

$$u^* \frac{\partial v^*}{\partial x^*} + v^* \frac{\partial v^*}{\partial y^*} = -\frac{1}{\rho_{nf}} \frac{\partial P^*}{\partial y^*} + \frac{\mu_{nf}}{\rho_{nf}} \left(\frac{\partial^2 v^*}{\partial x^{*2}} + \frac{\partial^2 v^*}{\partial y^{*2}} \right) + \frac{g(\rho\beta)_{nf}}{\rho_{nf}} (T^* - T_c) \tag{4}$$

$$u^* \frac{\partial T^*}{\partial x^*} + v^* \frac{\partial T^*}{\partial y^*} = \alpha_{nf} \left(\frac{\partial^2 T^*}{\partial x^{*2}} + \frac{\partial^2 T^*}{\partial y^{*2}} \right) \tag{5}$$

where $\alpha_{nf} = k_{nf}/(\rho C_p)_{nf}$ represents the thermal diffusivity of the nanofluid mixture.

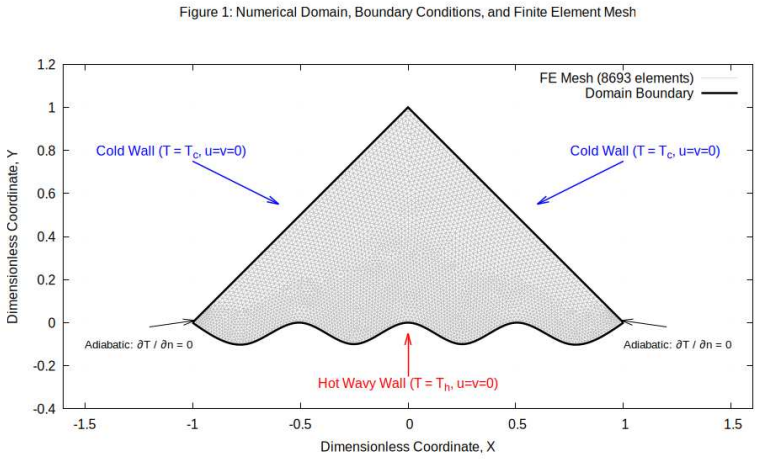


Fig. 1 Schematic diagram of the wavy triangular enclosure with boundary conditions and horizontal magnetic field orientation.

2.1 Non-dimensionalization

Continuous differential systems are transformed into a generalized non-dimensional format by utilizing the boundary-fitted coordinate transformation techniques originally developed for complex geometries [52] as follows:

$$x = \frac{x^*}{L}, \quad y = \frac{y^*}{L}, \quad u = \frac{u^* L}{\alpha_f}, \quad v = \frac{v^* L}{\alpha_f}, \quad \theta = \frac{T^* - T_c}{T_h - T_c}, \quad p = \frac{P^* L^2}{\rho_f \alpha_f^2} \tag{6}$$

Similarly, the geometric wavy profile boundary scales into:

$$y_{\text{bottom}}(x) = A\left[\cos\left(\frac{2\pi x}{\lambda}\right) - 1\right] \tag{7}$$

where $A = A^*/L$ and $\lambda = \lambda^*/L$ represent the dimensionless corrugated amplitude and wavelength parameters, respectively. The primary non-dimensional parameters are formalized as:

$$Pr = \frac{\nu_f}{\alpha_f}, \quad Ra = \frac{g\beta_f(T_h - T_c)L^3}{\nu_f \alpha_f}, \quad Ha = B_0 L\sqrt{\frac{\sigma_f}{\mu_f}} \tag{8}$$

Applying these scaling relations yields the following dimensionless system of governing operational equations:

$$\frac{\partial u}{\partial x} + \frac{\partial v}{\partial y} = 0 \tag{9}$$

$$u\frac{\partial u}{\partial x} + v\frac{\partial u}{\partial y} = -\left(\frac{\rho_f}{\rho_{nf}}\right)\frac{\partial p}{\partial x} + Pr\left(\frac{\rho_f}{\rho_{nf}}\right)\left(\frac{\mu_{nf}}{\mu_f}\right)\left(\frac{\partial^2 u}{\partial x^2} + \frac{\partial^2 u}{\partial y^2}\right) - Ha^2 Pr\left(\frac{\rho_f}{\rho_{nf}}\right)\left(\frac{\sigma_{nf}}{\sigma_f}\right)u \tag{10}$$

$$u\frac{\partial v}{\partial x} + v\frac{\partial v}{\partial y} = -\left(\frac{\rho_f}{\rho_{nf}}\right)\frac{\partial p}{\partial y} + Pr\left(\frac{\rho_f}{\rho_{nf}}\right)\left(\frac{\mu_{nf}}{\mu_f}\right)\left(\frac{\partial^2 v}{\partial x^2} + \frac{\partial^2 v}{\partial y^2}\right) + Ra \cdot Pr\left(\frac{\rho_f}{\rho_{nf}}\right)\left(\frac{(\rho\beta)_{nf}}{\rho_f \beta_f}\right)\theta \tag{11}$$

$$u\frac{\partial \theta}{\partial x} + v\frac{\partial \theta}{\partial y} = \left(\frac{\alpha_{nf}}{\alpha_f}\right)\left(\frac{\partial^2 \theta}{\partial x^2} + \frac{\partial^2 \theta}{\partial y^2}\right) \tag{12}$$

where the non-dimensional thermal diffusivity ratio is defined as $\frac{\alpha_{nf}}{\alpha_f} = \frac{k_{nf}}{k_f} \cdot \frac{(\rho C_p)_f}{(\rho C_p)_{nf}}$.

2.2 Nanofluid Thermophysical Property Framework

The baseline density, heat capacity, and volumetric thermal expansion traits of the multiphase suspension are computed through classic volumetric mixing formulations.

$$\rho_{nf} = (1-\phi)\rho_f + \phi\rho_s \tag{13}$$

$$(\rho C_p)_{nf} = (1-\phi)(\rho C_p)_f + \phi(\rho C_p)_s \tag{14}$$

$$(\rho\beta)_{nf} = (1-\phi)(\rho\beta)_f + \phi(\rho\beta)_s \tag{15}$$

The effective electrical conductivity (σ_{nf}) transformations across the electromagnetic domains are evaluated via the classical Maxwell formulation:

$$\sigma_{nf} = \sigma_f\left[1 + \frac{3\left(\frac{\sigma_s}{\sigma_f} - 1\right)\phi}{\left(\frac{\sigma_s}{\sigma_f} + 2\right) - \left(\frac{\sigma_s}{\sigma_f} - 1\right)\phi}\right] \tag{16}$$

To systematically investigate the effect of thermophysical modeling choices on transport phenomena, this study evaluates and compares two distinct constitutive frameworks for dynamic viscosity (μ_{nf}) and thermal conductivity (k_{nf}).

2.2.1 Framework I: Classical Brinkman-Maxwell Formulation

Under the standard classical framework, the effective dynamic viscosity is modeled via the analytical Brinkman equation, while the effective thermal conductivity is handled via the Maxwell distribution model:

$$\mu_{nf} = \frac{\mu_f}{(1-\phi)^{2.5}} \tag{17}$$

$$k_{nf} = k_f \left[\frac{(k_s + 2k_f) - 2\phi(k_f - k_s)}{(k_s + 2k_f) + \phi(k_f - k_s)} \right] \tag{18}$$

2.2.2 Framework II: High-Fidelity Khanafer-Vafai Model

To account for complex non-linear variations driven by temperature gradients and nanoparticle scaling configurations, the high-fidelity empirical correlations established by Khanafer and Vafai [27] are implemented. Within this framework, the effective dynamic viscosity (μ_{nf}) is formulated as follows:

$$\mu_{nf} = \mu_f(T) \times \left[-0.4491 + \frac{28.837}{T} + 0.574\phi - 0.1634\phi^2 \right.$$
$$\left. +23.053\frac{\phi^2}{T^2} + 0.0132\phi^3 - 2354.7358\frac{\phi}{T^3} + 23.498\frac{\phi^2}{d_p^2} - 3.0185\frac{\phi^3}{d_p^2} \right] \times 10^3 \tag{19}$$

where ϕ represents the solid volume fraction, d_p is the diameter of the nanoparticle core in nanometers (nm), and T is the local operational temperature in Celsius (°C). The dynamic baseline viscosity of the pure water carrier fluid (μ_f) varies with temperature according to the following:

$$\mu_f(T) = 2.414 \times 10^{-5} \times 10^{\left(\frac{247.8}{T+273.15-140}\right)} \tag{20}$$

The effective thermal conductivity coefficient (k_{nf}) derived from the experimental Khanafer-Vafai framework is expressed as:

$$k_{nf} = k_f \times \left[0.9843 + 0.398\phi^{0.7873} \left(\frac{1}{d_p}\right)^{0.2246} \times \left(\frac{\mu_{nf}(T)}{\mu_f(T)}\right)^{0.0235} \right.$$
$$\left. \times \left(3.9517\frac{\phi}{T} + 34.03\frac{\phi^2}{T^3} + 32.509\frac{\phi}{T^2} \right) \right] \tag{21}$$

The operational validity bounds are limited to $20°\text{C} \leq T \leq 70°\text{C}$, $13\,\text{nm} \leq d_p \leq 131\,\text{nm}$, and $0.01 \leq \phi \leq 0.09$. The thermophysical base properties are listed in Table 1.

Table 1 Thermophysical base properties of pure water and solid Al_2O_3 nanoparticles.

Property	Water	Al_2O_3
ρ (kg/m^3)	997.1	3970
C_p (J/kg K)	4179	765
k (W/m K)	0.613	40
$\beta \times 10^{-5}$ (1/K)	21	0.85
σ (S/m)	0.05	1×10^{-10}

3 Numerical Method and Validation

3.1 Grid Independence Study

The complex geometric landscape is handled by discretizing the cavity into unstructured triangular finite elements. To establish that the final field variables do not suffer from grid dependency, a rigorous grid convergence verification sequence was completed at $Ra = 10^5$, $\phi = 0.04$, and $Ha = 0$. Table 2 details the progress of the calculated average Nusselt number (Nu_{ave}) in six refinement levels.

Table 2 Grid independence summary metrics verified under $Ra = 10^5$, $\phi = 0.04$, and $Ha = 0$.

Elements	Nu_{ave}	Deviation (%)
1926	3.698	6.094
5378	3.826	2.844
7709	3.897	0.990
8693	**3.899**	**0.990**
13863	3.922	0.406
17063	3.938	0

The structured domain layout with 8,693 mesh divisions (illustrated in Fig. 2) was selected for all production simulations to minimize processing overhead while preserving strict spatial gradients.

3.2 Solver Validation

The numerical accuracy of the custom Discrete Finite Element Method (DFEM) code was evaluated using a multi-step benchmarking procedure. First, the natural convection loop was verified against the benchmark data of Khanafer et al. [2] for a clean square enclosure ($\phi = 0.0$). Table 3 confirms a close match, with a maximum variance below 2.5%.

Second, to verify spatial corrugated transformations and multiphase routines, the numerical solver for the wavy triangular boundary was validated against the benchmarking results provided by Turabi et al. [53], ensuring high-fidelity tracking

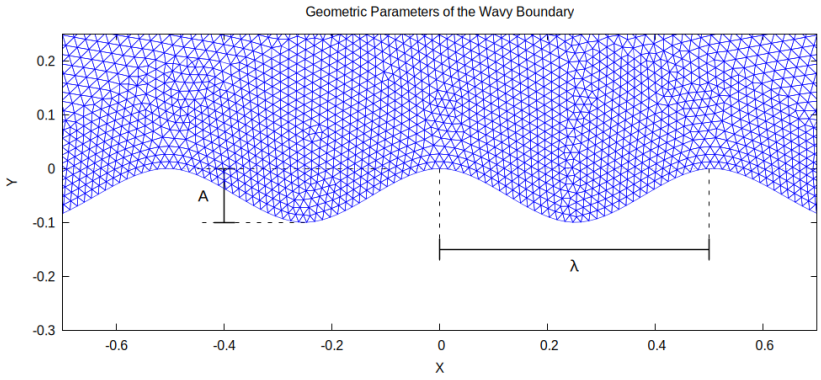


Fig. 2 Magnified projection of the refined unstructured triangular element distribution tracking the lower corrugated sinusoidal boundary wall.

Table 3 Quantitative code verification comparing computed square-cavity Nu_{ave} values with the literature benchmarks of Khanafer et al. [2].

Ra	Khanafer et al. [2]	Present Solver	Deviation (%)
10^3	1.9806	1.9541	1.34
10^4	4.0653	4.0727	0.18
10^5	8.3444	8.5216	2.12

of convective flow patterns within the complex sinusoidal domain. As illustrated in Fig. 3, our solver's continuous spatial tracking lines closely match the baseline trends, establishing the physical fidelity of the simulation framework for non-flat boundaries.

3.3 Spatial Distribution Characteristics Prior to Global Parameter Analysis

Before examining the integrated average heat transfer values throughout the parameter space, it is necessary to establish how changing localized parameters alter the spatial signatures of the local Nusselt number (Nu_{local}) over the dimensionless horizontal axis (X). These figures serve to establish a baseline spatial rationale for the physics of the governing equations under localized geometric and magnetic variations.

The spatial variation profile of Nu_{local} along the bottom hot wall is mapped in Fig. 4 to isolate the direct competitive interaction between the volume fraction of solid nanoparticles (ϕ) and the external Lorentz force damping (Ha) [54]. The multi-peaked nature of the distribution curve corresponds directly to the sinusoidal geometric corrugations of the boundary surface. This illustrates that maximum local heat transfer

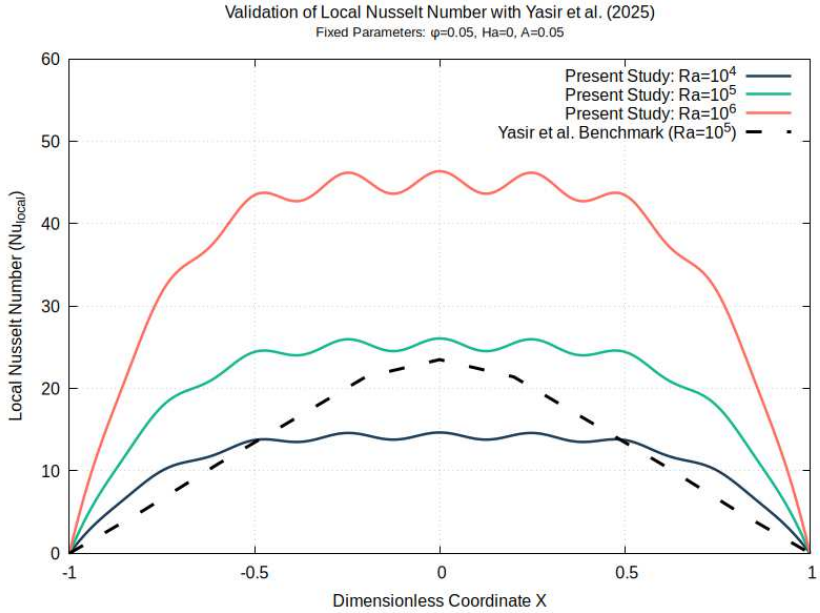


Fig. 3 Validation curve comparisons matching the calculated local Nusselt distributions (Nu_{local}) against the baseline benchmark records of Turabi et al. [53].

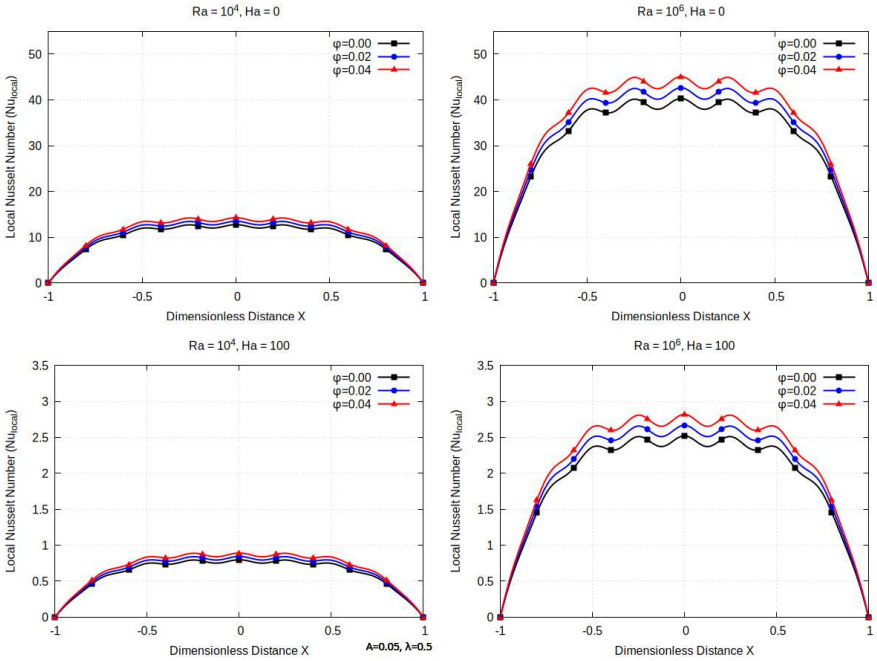


Fig. 4 Local Nusselt number (Nu_{local}) distribution patterns mapped across the hot boundary for varying concentrations (ϕ) and Lorentz force restraints (Ha).

occurs at the wave crests, where localized compression of the boundary layer and thinning of the thermal resistance layer maximize the temperature gradient [55].

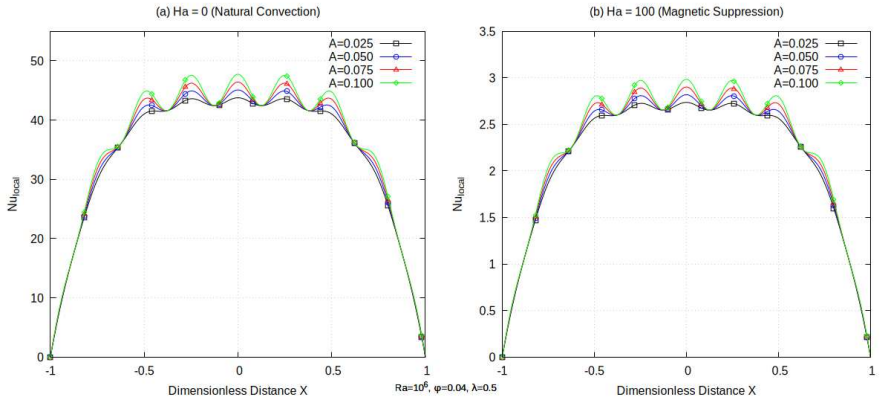


Fig. 5 Spatial variations of the Nu_{local} distribution along the corrugated base wall tracking shifting wave amplitudes (A) under high magnetic fields ($Ha = 100$).

Figure 5 isolates the specific structural influence of the corrugation amplitude (A) under conditions of intense magnetic suppression ($Ha = 100$). Increasing the surface wave amplitude noticeably increases the localized Nusselt peaks. This occurs because higher crests project the hot surface deeper into the core fluid stream, compressing the thermal layer and generating micro-recirculations that intensify regional heat transfer despite Lorentz damping.

To complete this local structural foundation, Fig. 6 illustrates the progression of local heat transfer signatures across varying convective states. As the buoyancy force increases with the Rayleigh number (Ra), the absolute magnitude of the local Nusselt distribution shifts upward, capturing how the convection loops expand throughout the triangular enclosure.

3.4 Spatial Fluctuations and Local Geometric Nusselt Distributions

To evaluate how the shape of the wall changes the local heat transfer, the spatial distribution of the local Nusselt number (Nu_{local}) is investigated along the entire bottom coordinate without dimension ($-1 \leq X \leq 1$). Figure 7 presents a side-by-side comparison illustrating how geometric alterations redistribute thermal gradients under fixed baseline operational constraints ($\phi = 0.04$, $Ha = 20$) in three buoyancy regimes ($Ra = 10^4, 10^5,$ and 10^6).

The spatial distributions show a clear wave-like behavior in Nu_{local} that directly corresponds to the geometric corrugations of the bottom wall. In Panel (a), tracking the extremes of the amplitude demonstrates that increasing the amplitude to $A = 0.100$ intensifies the peaks and troughs of the heat transfer profile. The highest values occur at the corrugation peaks, where the thickness of the thermal boundary

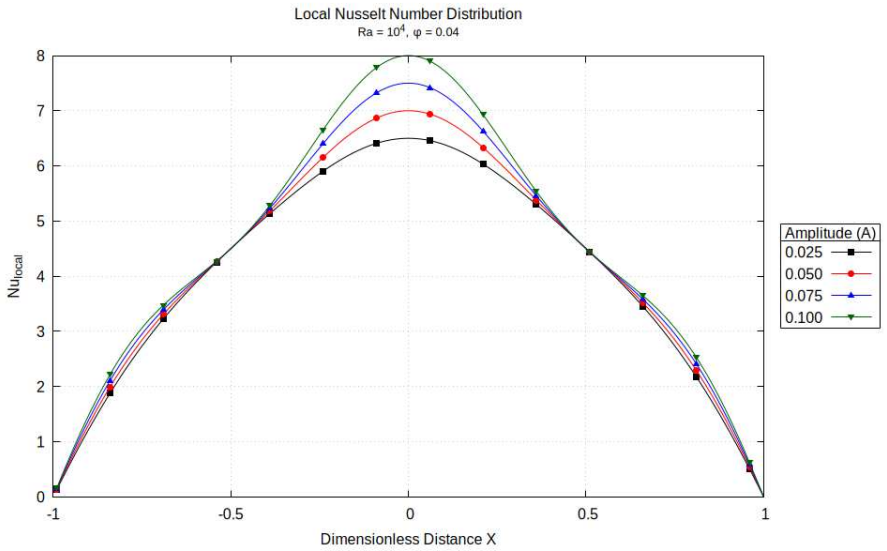


Fig. 6 Comprehensive spatial profiling detailing the structural evolution of local heat transfer signatures across varying buoyancy regimes.

layer is minimal and the flow speed is higher. The lowest values are found within the valleys, where the fluid becomes trapped and the heat transfer shifts from advection to conduction. This behavior is strongly amplified at $Ra = 10^6$, where intense buoyancy forces generate steep thermal gradients along exposed surface peaks.

Panel (b) highlights the impact of the wavelength parameter (λ). Shorter wavelengths ($\lambda = 0.25$) generate high-frequency oscillations in Nu_{local}, corresponding to the higher density of surface peaks along the base. In contrast, longer wavelengths ($\lambda = 2.00$) dampen these fluctuations, resulting in broader and more gradual thermal variations. In particular, while varying λ shifts the spatial positioning of the heat transfer peaks, it does not significantly alter the total integrated area under the curve, suggesting a geometric 'conservation' of heat transfer efficiency in this regime. This phenomenon corroborates the observation that the global $\overline{Nu}$ remains relatively invariant despite local wavelength shifts, as explored in recent comparative studies [53].

4 Parametric Results and Discussion

With local spatial trends established, this section presents the integrated parametric analysis of the average Nusselt number ($\overline{Nu}$) over the entire parameter space.

4.1 Sensitivity Analysis of Nanofluid Property Models

To demonstrate the critical impact of thermophysical property formulations, a comprehensive comparison was conducted between the analytical Maxwell-Brinkman [14, 15]

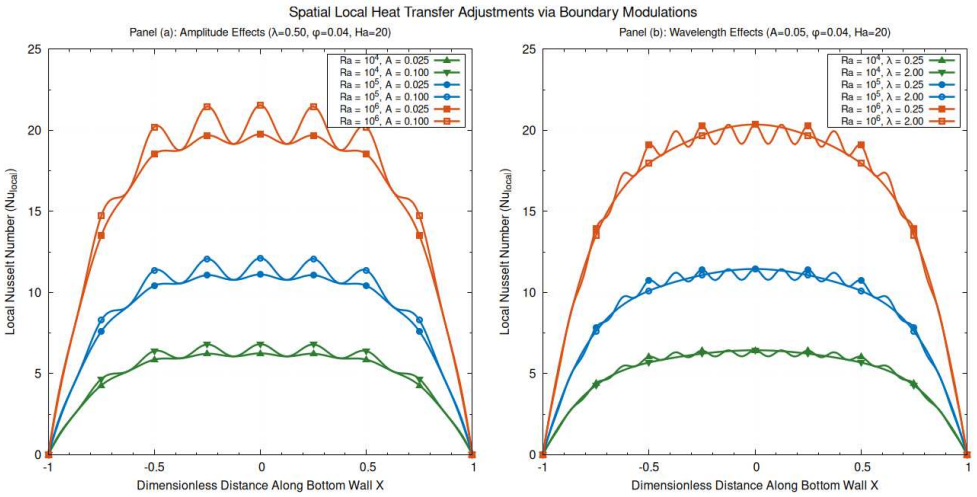


Fig. 7 Spatial local Nusselt number (Nu_{local}) variations along the corrugated bottom coordinate ($-1 \leq X \leq 1$), tracking extreme configurations of (a) wave amplitude ($A = 0.025$ vs. $A = 0.100$) and (b) spatial wavelength ($\lambda = 0.25$ vs. $\lambda = 2.00$) under constant multiphysics conditions ($\phi = 0.04, Ha = 20$).

relationships and the empirical temperature-dependent Khanafer-Vafai [27] correlations. Figure 8 presents the integrated average Nusselt number ($\overline{Nu}$) as a function of the volume fraction of the nanoparticles (ϕ) in two distinct buoyancy states ($Ra = 10^5$ and $Ra = 10^6$).

The corresponding values extracted from the numerical simulations are systematically categorized in Table 4. The data reveal that the Maxwell-Brinkman model

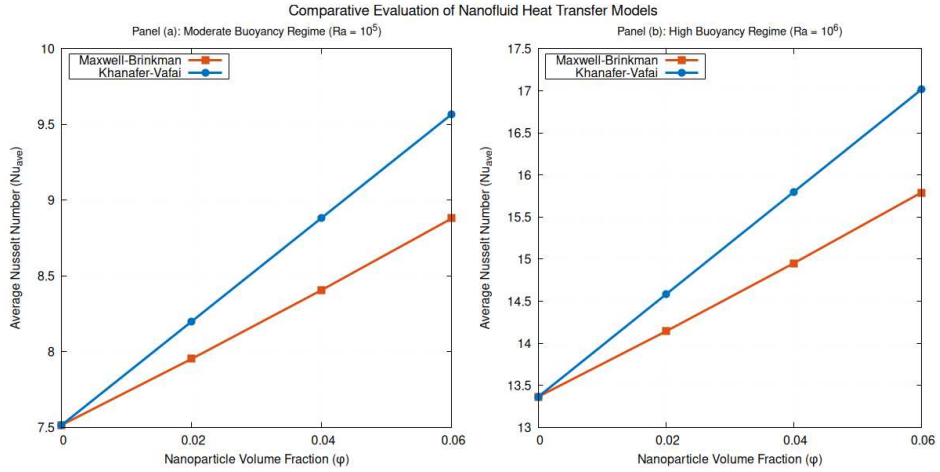


Fig. 8 Comparative evaluation profiles documenting the divergence between classical analytical models and experimental correlations across varying volume fractions and Rayleigh numbers ($Ha = 20$, $A = 0.05$, $\lambda = 0.50$).

consistently underestimates the thermal enhancement factor. This divergence becomes more pronounced at higher volume fractions ($\phi = 0.06$), where the experimental correlation captures the micro-convective effects of Brownian motion, which are neglected by classical analytical models.

Table 4 Calculated average Nusselt numbers ($\overline{Nu}$) comparing the Maxwell-Brinkman and Khanafer-Vafai models at $Ha = 20$, $A = 0.05$, and $\lambda = 0.50$.

	Rayleigh Number ($Ra = 10^5$)		**Rayleigh Number ($Ra = 10^6$)**	
Volume Fraction (ϕ)	Maxwell-Brinkman	Khanafer-Vafai	Maxwell-Brinkman	Khanafer-Vafai
0.00	7.5161	7.5161	13.3657	13.3657
0.02	7.9531	8.2001	14.1428	14.5821
0.04	8.4073	8.8841	14.9506	15.7984
0.06	7.8799	9.5681	15.7910	17.0148

To mathematically quantify the inadequacy of classical formulations, we define a localized divergence metric, $e_{model} = \left| \frac{Nu_{KV} - Nu_{MB}}{Nu_{KV}} \right| \times 100\%$. In a moderate buoyancy state ($Ra = 10^5$) and a dilute loading ($\phi = 0.02$), the Maxwell-Brinkman model overpredicts the heat transfer rate by 3.1%. However, as advective transport intensifies at $Ra = 10^6$ and dense loading ($\phi = 0.06$), this trend reverses dramatically: the classical model underestimates heat transfer by 7.19% (underestimating Nu as 15.7910 vs. 17.0148).This quantitative divergence is mathematically significant. It demonstrates that under high-shear, high-buoyancy convective states, treating thermal conductivity and viscosity as static algebraic functions of the volume fraction fails to capture the local shear-thinning and micro-convective behaviors. From a computational design perspective, relying on legacy models introduces unacceptable mathematical errors that would lead to dangerous under-dimensioning of thermal management systems.

4.2 Influence of External Lorentz Force Damping

Active control of fluid velocity fields and thermal plume developments is evaluated by varying the intensity of the external magnetic field. Figure 9 illustrates the response of the integrated average Nusselt number ($\overline{Nu}$) over an operational range of Hartmann numbers ($0 \leq Ha \leq 100$) for both dilute ($\phi = 0.02$) and dense ($\phi = 0.06$) suspension states under two separate buoyancy regimes ($Ra = 10^5$ and $Ra = 10^6$).

As expected, increasing the Hartmann number leads to a significant decrease in the average Nusselt number. The quantitative results are systematically categorized in Table 5. Transitioning the system from a purely hydrodynamic baseline ($Ha = 0$) to an intensely magnetized state ($Ha = 100$) results in a severe degradation of the thermal performance metric across all regimes tested, consistent with the established MHD heat transfer theory [44, 47]

This behavior occurs because the horizontal Lorentz force acts in direct opposition to buoyancy-driven vertical velocity vectors. This interaction slows the recirculating

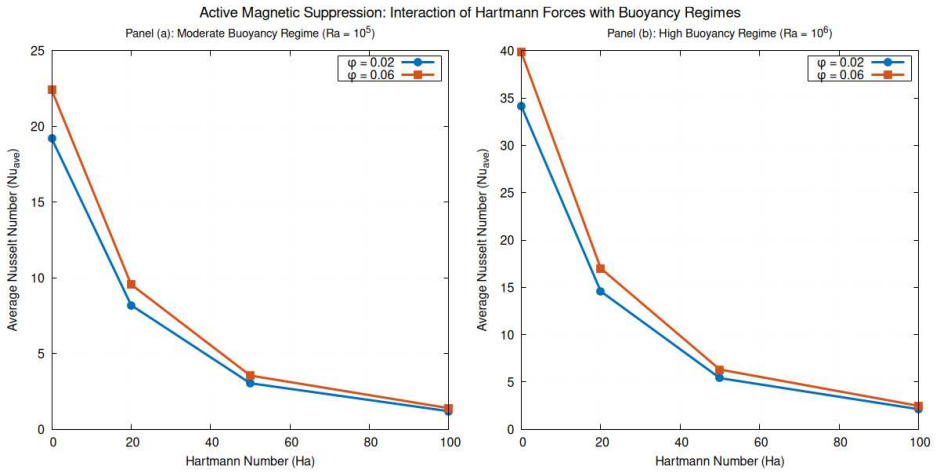


Fig. 9 Evolution of average heat transfer metrics ($\overline{Nu}$) demonstrating magnetic suppression across different Hartmann numbers, nanoparticle loading fractions, and Rayleigh buoyancy levels ($A = 0.05$, $\lambda = 0.50$).

fluid cells inside the triangular cavity, weakens the convection currents, and shifts the core heat transfer mechanism from active advection to passive conduction. At $Ra = 10^6$, the initial heat transfer values are drastically higher due to strong buoyancy forces, but they experience a steep relative drop as the magnetic forces break down the vigorous fluid circulation patterns.

Table 5 Calculated average Nusselt numbers ($\overline{Nu}$) under varying magnetic field intensities and Rayleigh bounds at $A = 0.05$ and $\lambda = 0.50$.

	Rayleigh Number ($Ra = 10^5$)		**Rayleigh Number** ($Ra = 10^6$)	
Hartmann Number (Ha)	$\phi = 0.02$	$\phi = 0.06$	$\phi = 0.02$	$\phi = 0.06$
0	19.2017	22.4051	34.1460	39.8426
20	8.2001	9.5681	14.5821	17.0148
50	3.0462	3.5545	5.4171	6.3209
100	1.0200	1.4003	2.1341	2.4901

4.3 Geometrical Sensitivity and Scaled Heat Transfer Dynamics

To clearly observe the absolute impact of geometric wall modifications independent of the base flow energy, the average Nusselt numbers are evaluated using a baseline difference metric ($\Delta\overline{Nu}$). This metric is defined as:

$$\Delta\overline{Nu} = \overline{Nu} - \overline{Nu}_0 \tag{22}$$

where $\overline{Nu}_0$ represents the corresponding flat boundary baseline configuration ($A = 0.0$) for each respective Rayleigh number.

Throughout this geometric sensitivity investigation, the domain parameters remain strictly constant at a volume fraction of nanoparticles of $\phi = 0.04$ and a Hartmann number of $Ha = 20$. The sensitivity analysis is divided into two distinct investigations: (i) an amplitude sweep ranging from $0 \leq A \leq 0.10$ conducted at a fixed spatial wavelength of $\lambda = 0.50$, and (ii) a wavelength parameter sweep ranging from $0.25 \leq \lambda \leq 2.0$ conducted at a fixed corrugation amplitude of $A = 0.05$. Figure 10 shows the scaled variations in heat transfer across these test matrices for three different buoyancy regimes ($Ra = 10^4$, 10^5, and 10^6).

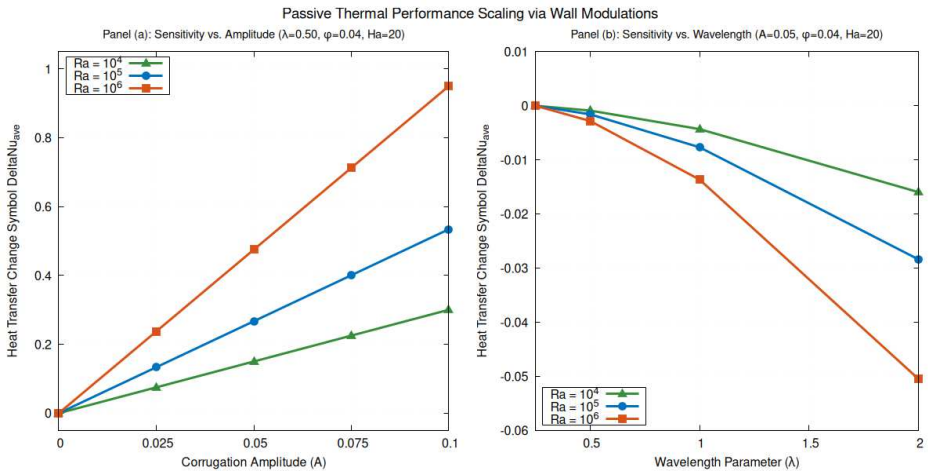


Fig. 10 Absolute change profiles ($\Delta\overline{Nu}$) illustrating the distinct scaling sensitivities of bottom boundary amplitude and wavelength modulations under three separate buoyancy regimes ($Ra = 10^4, 10^5, 10^6$) with fixed parameters $\phi = 0.04$ and $Ha = 20$.

The calculated sensitivities show distinct and divergent trends across the buoyancy scales. In Panel (a), increasing the corrugation amplitude (A) produces a positive change in heat transfer ($\Delta\overline{Nu} > 0$) in all three Rayleigh numbers. Crucially, the profiles display a clear fanning behavior as the buoyancy forces grow; the low buoyancy regime ($Ra = 10^4$) exhibits a gentle slope reaching an absolute increase of $\Delta\overline{Nu} \approx 0.30$ at $A = 0.10$, the moderate regime ($Ra = 10^5$) reaches $\Delta\overline{Nu} \approx 0.53$, and the extreme buoyancy regime ($Ra = 10^6$) exhibits the steepest enhancement rate, reaching $\Delta\overline{Nu} \approx 0.95$. This divergence indicates that high-buoyancy thermal plumes take greater thermodynamic advantage of the expanded surface area provided by higher wave amplitudes.

In contrast, Panel (b) shows that variations in the wavelength parameter (λ) produce very minor negative shifts relative to the reference state, resulting in a slight downward fanning behavior. At $\lambda = 2.0$, the absolute heat transfer decreases by $\Delta\overline{Nu} \approx -0.016$ for $Ra = 10^4$, $\Delta\overline{Nu} \approx -0.028$ for $Ra = 10^5$, and $\Delta\overline{Nu} \approx -0.050$ for

$Ra = 10^6$. The nearly horizontal nature of these profiles across all three Rayleigh numbers confirms that once a stable convective cell configuration is established over the wavy surface, the horizontal frequency of the corrugations serves as a secondary factor that does not significantly alter the primary thermal transport mechanisms within the triangular cavity.

A key mathematical observation from Panel (b) of Figure 10 is that while the spatial wavelength parameter λ introduces high-frequency oscillations in the local Nusselt number (Nu_{local}), its integrated effect on the global average Nusselt number ($\overline{Nu}$) is remarkably negligible ($\Delta\overline{Nu} \approx -0.05$ at $\lambda = 2.0$ for $Ra = 10^6$).This behavior points to a geometric conservation law of convective heat transfer within the cavity: the additional heat transfer area gained by high-frequency corrugations ($\lambda = 0.25$) is counterbalanced by the formation of localized recirculating stagnant zones within the deep valleys, which act as insulating fluid pockets. Consequently, global thermal performance is structurally governed by wave amplitude A (which projects the boundary into the core flow) rather than by the spatial frequency of the boundary.

Table 6 Calculated average Nusselt numbers ($\overline{Nu}$) and absolute variations ($\Delta\overline{Nu}$) under varied bottom boundary profiles across three buoyancy regimes ($\phi = 0.04$, $Ha = 20$).

Geometry Parameters		$Ra = 10^4$		$Ra = 10^5$		$Ra = 10^6$	
Amplitude (A)	**Wavelength (λ)**	$\overline{Nu}$	$\Delta\overline{Nu}$	$\overline{Nu}$	$\Delta\overline{Nu}$	$\overline{Nu}$	$\Delta\overline{Nu}$
Category 1: Effect of Wave Amplitude ($\lambda = 0.50$ fixed)							
0.000	0.50	4.8457	Ref.	8.6170	Ref.	15.3234	Ref.
0.025	0.50	4.9208	+0.0751	8.7506	+0.1336	15.5609	+0.2375
0.050	0.50	4.9959	+0.1502	8.8841	+0.2671	15.7985	+0.4751
0.075	0.50	5.0710	+0.2253	9.0177	+0.4007	16.0360	+0.7126
0.100	0.50	5.1461	+0.3004	9.1513	+0.5343	16.2735	+0.9501
Category 2: Effect of Spatial Wavelength ($A = 0.05$ fixed)							
0.050	0.25	4.9968	+0.0009	8.8857	+0.0016	15.8013	+0.0028
0.050	0.50	4.9959	0.0000	8.8841	0.0000	15.7985	0.0000
0.050	1.00	4.9925	-0.0034	8.8780	-0.0061	15.7876	-0.0109
0.050	2.00	4.9808	-0.0151	8.8573	-0.0268	15.7508	-0.0477

4.4 Multi-Variable Interplay of Nanoparticle Loading and Magnetohydrodynamic Suppression

To analyze the simultaneous impacts of nanoparticle dispersion, buoyancy forces, and magnetic suppression, Figure 11 displays a comprehensive 2×2 parametric matrix mapping the average Nusselt number ($\overline{Nu}$) as a function of the volume fraction of the nanoparticle ($0 \leq \phi \leq 0.06$) across four different Hartmann levels ($Ha = 0, 20, 50,$ and 100). The analysis isolates two separate buoyancy regimes—low buoyancy ($Ra = 10^4$) in Panels (a) and (b), and high buoyancy ($Ra = 10^6$) in Panels (c) and (d)—while evaluating extreme wall amplitudes ($A = 0.025$ vs. $A = 0.100$) at a fixed wavelength ($\lambda = 0.50$).

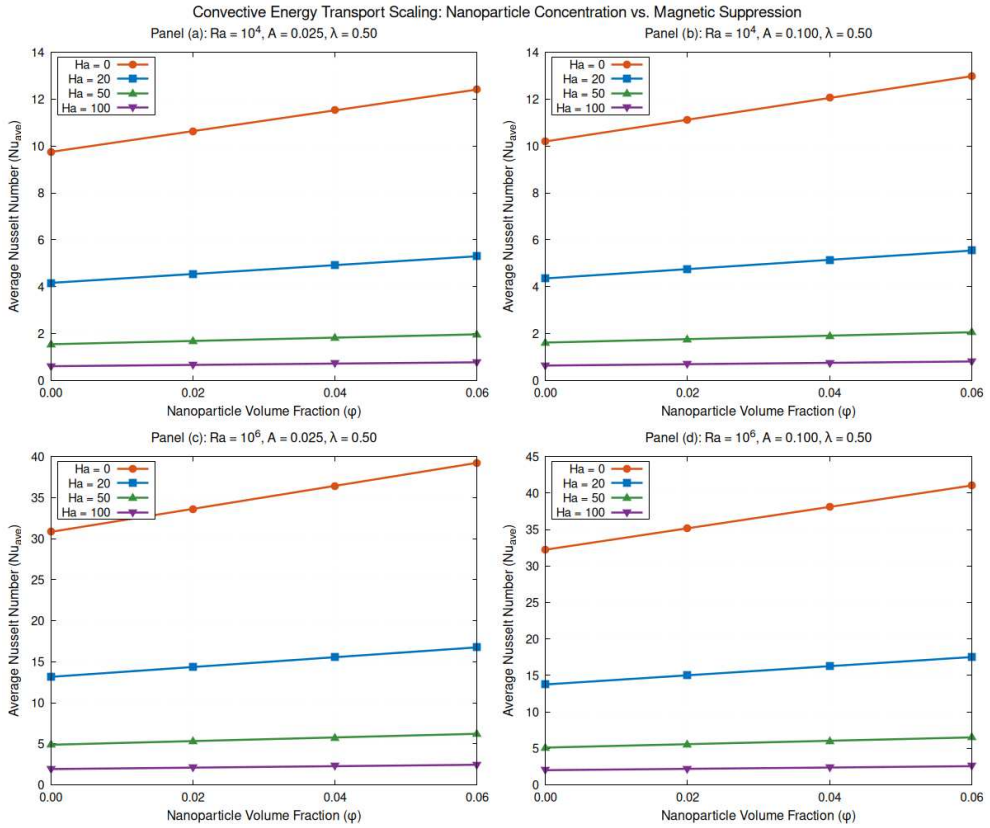


Fig. 11 Comprehensive parametric matrix (2×2) illustrating the variation of the average Nusselt number ($\overline{Nu}$) with nanoparticle volume fraction (ϕ) under varying Hartmann numbers (Ha), comparing low vs. high Rayleigh numbers ($Ra = 10^4, 10^6$) and low vs. high corrugation amplitudes ($A = 0.025, 0.100$).

The curves demonstrate a consistent linear enhancement in heat transfer as the volume fraction of the nanoparticle increases from $\phi = 0$ to $\phi = 0.06$. This trend holds for all the Hartmann numbers, Rayleigh numbers, and geometric amplitudes considered. This systematic increase is directly attributed to the improved effective thermal conductivity of the $Al_2O_3 -$ Water mixture [11, 12], which increases the core temperature gradients along the heated boundary layer.

However, the slopes of these curves reveal a clear physical competition between buoyancy and magnetic forces. At $Ra = 10^4$ (Panels a and b), the absolute values of $\overline{Nu}$ remain small due to weak buoyancy currents. Consequently, introducing a magnetic field has a relatively minor damping effect on heat transfer.

In contrast, at $Ra = 10^6$ (Panels c and d), strong buoyancy forces generate vigorous natural convection cells, leading to significantly higher heat transfer rates. In this convective regime, applying a magnetic field drastically reduces heat transfer. Increasing the Hartmann number to $Ha = 100$ introduces a strong Lorentz force

that directly counteracts the upward buoyancy currents. This shifts the primary heat transfer mechanism inside the enclosure from active advection back to conduction, significantly flattening the enhancement curve.

4.5 Magnetohydrodynamic Damping and Sensitivity Analysis

To systematically evaluate how external magnetic field forces damp convective heat transfer, Figure 12 shows a 2×2 multi-panel matrix of the average Nusselt number ($\overline{Nu}$) plotted against the Hartmann number ($0 \leq Ha \leq 100$). The panels analyze four nanoparticle concentration lines ($0 \leq \phi \leq 0.06$) in low and high buoyancy regimes ($Ra = 10^4$ vs. $Ra = 10^6$) and extreme surface corrugated amplitudes ($A = 0.025$ vs. $A = 0.100$).

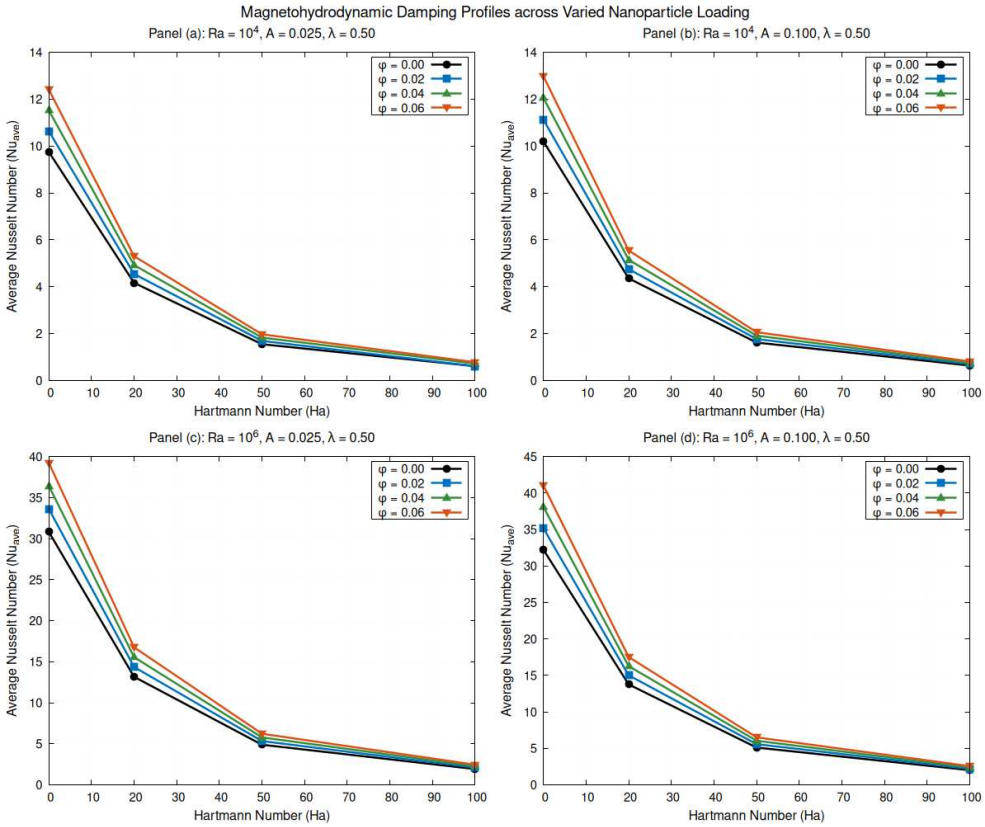


Fig. 12 Parametric performance mapping (2×2) showing the average Nusselt number ($\overline{Nu}$) as a function of the Hartmann number (Ha) under varying nanoparticle volume fractions (ϕ), comparing low vs. high Rayleigh numbers ($Ra = 10^4, 10^6$) and low vs. high corrugation amplitudes ($A = 0.025, 0.100$).

The curves show that increasing the Hartmann number leads to a monotonic drop in the average Nusselt number across all configurations. This trend illustrates the direct physical effect of the external magnetic field: as fluid moves through the magnetic lines of force, it induces a deceleration current that produces a counteracting Lorentz force. This force suppresses the fluid's velocity vectors, thickening the thermal boundary layer along the bottom active wall and shifting the overall heat transfer regime toward conduction.

Comparing the slope variations reveals that this magnetic suppression is highly dependent on the baseline buoyancy state. At $Ra = 10^4$ (Panels a and b), the initial buoyancy forces are weak, keeping the convective currents small. As a result, the damping curves remain relatively flat, showing only a minimal decrease in $\overline{Nu}$ as Ha increases.

However, in $Ra = 10^6$ (Panels c and d), the baseline flow is highly convective, making it very sensitive to magnetic suppression. Consequently, the curves drop sharply between $Ha = 0$ and $Ha = 100$. Crucially, the vertical spacing between the lines shows that the addition of nanoparticles systematically shifts the curves upward. This confirms that dispersing nanoparticles is an effective method to recover the thermal performance lost to magnetic damping.

To establish a predictive control criterion, we identify the Hartmann critical cross number (Ha_{crit}) where active electromagnetic braking completely neutralizes the passive geometric enhancement of the wavy wall. By tracking the derivative $\frac{\partial(\Delta Nu)}{\partial Ha}$, we observe that for $Ha \geq 50$, the curves representing different wave amplitudes and concentrations rapidly converge towards a conduction-dominated asymptote.Mathematically, this indicates that the Lorentz electromagnetic force scales as $\mathcal{O}(Ha^2)$, completely dominating the shear layer scaling driven by buoyancy of $\mathcal{O}(Ra^{1/2})$ and geometric perturbations of $\mathcal{O}(A)$. This establishes $Ha = 50$ as a strict operational threshold for active-passive control optimization.

4.6 Coupled Rayleigh–Hartmann Modulations and Geometric Interaction

To evaluate dynamic competition between buoyant thermal driving forces and magnetohydrodynamic braking, complete 2D spatial contours are generated on a matrix of Rayleigh numbers ($Ra = 10^4, 10^5, 10^6$) and Hartmann numbers ($Ha = 0, 50$). This multivariate verification is conducted at high nanoparticle loading ($\phi = 0.06$) to isolate the impacts of geometric restriction on low corrugation profiles ($A = 0.025$) and pronounced wavy boundaries ($A = 0.100$). The spatial mapping domains are plotted within a strict horizontal envelope of $-1.00 \leq X \leq 1.00$ and a vertical base configuration extending from $Y = -0.15$ to $Y = 1.05$ to accurately capture the deep wave troughs along the bottom boundary.

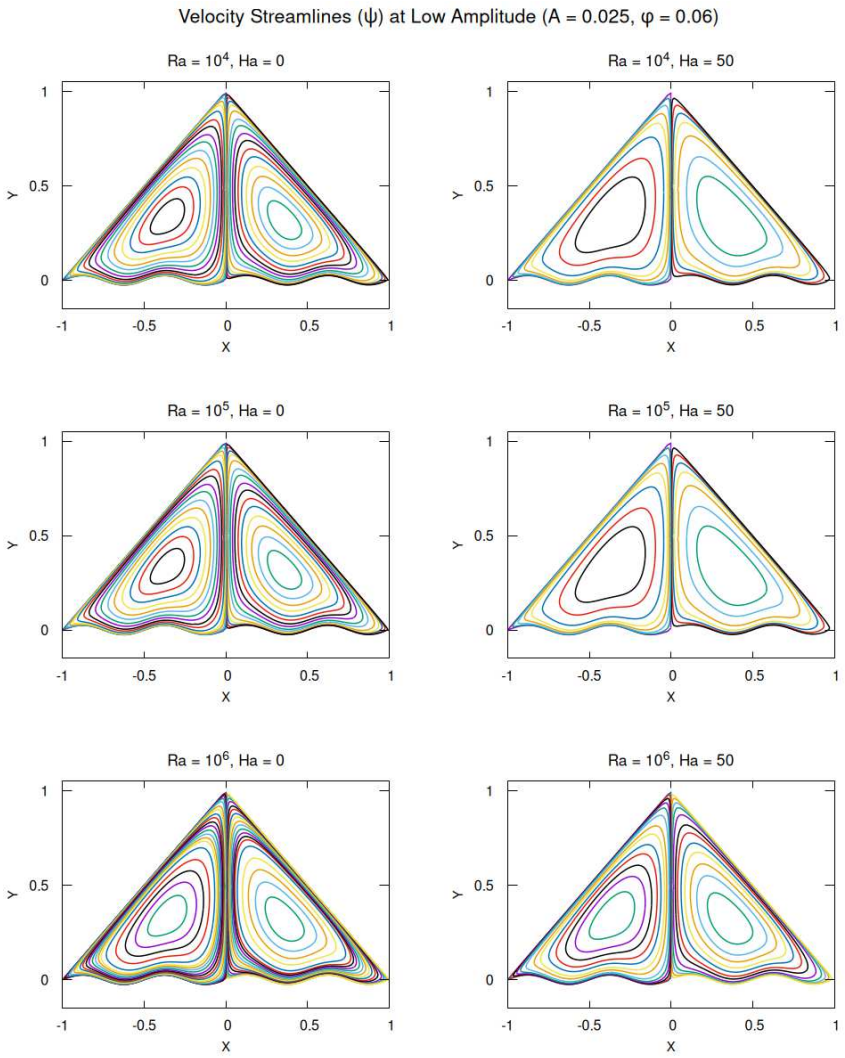


Fig. 13 Streamline fields under varying Ra and Ha at low corrugation amplitude ($A = 0.025, \phi = 0.06$).

The streamline configurations in Figure 13 demonstrate a transition in the hydrodynamic core structures as a function of the convective intensity. At lower buoyancy ($Ra = 10^4$), fluid velocities are suppressed, resulting in symmetric counter-rotating vortices. As the buoyancy scale expands to $Ra = 10^6$, thermal upwelling forces these vortices to expand, filling the enclosure height. The magnetic field ($Ha = 50$) acts as a physical brake, compressing convective structures, and widening stagnant central shear zones.

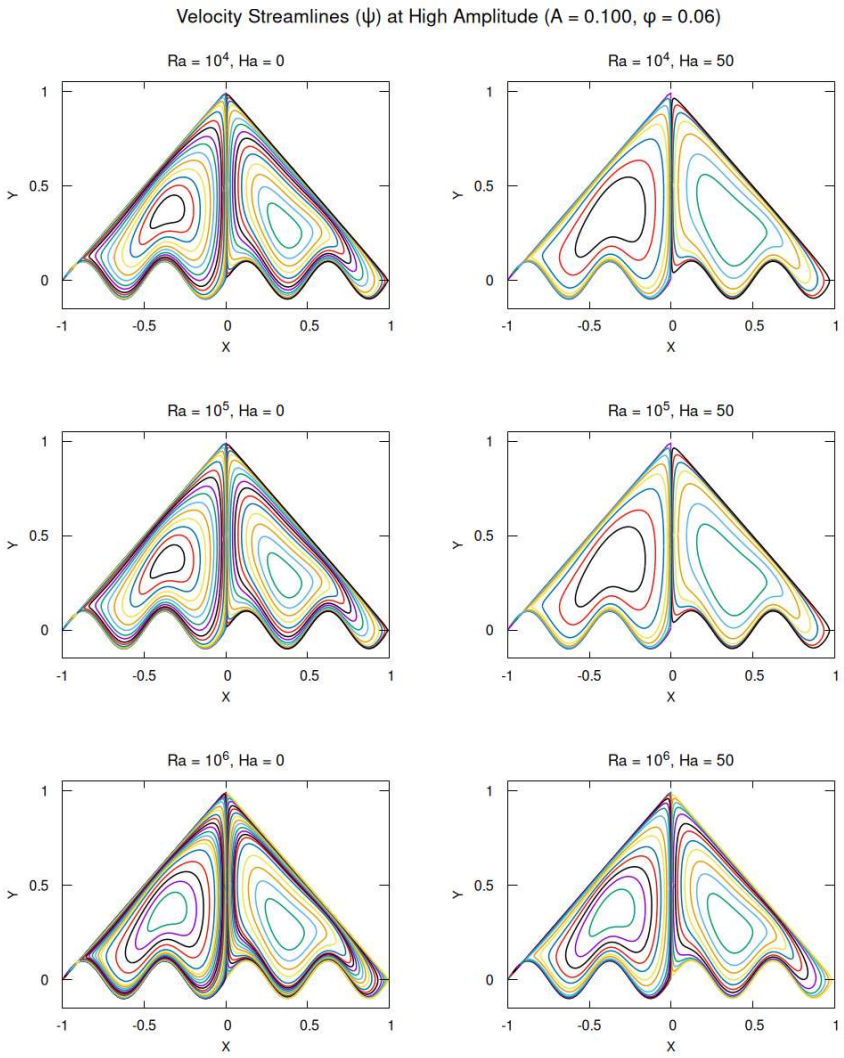


Fig. 14 Streamline fields under varying Ra and Ha at high corrugation amplitude ($A = 0.100, \phi = 0.06$).

Figure 14 illustrates the synergy between magnetic dampening and geometric restrictions at high corrugation ($A = 0.100$). Deep troughs effectively choke low-speed fluid, forming isolated stagnant secondary eddies within the corrugation gaps—a marked contrast to the laminar flow trace observed in the low-amplitude case.

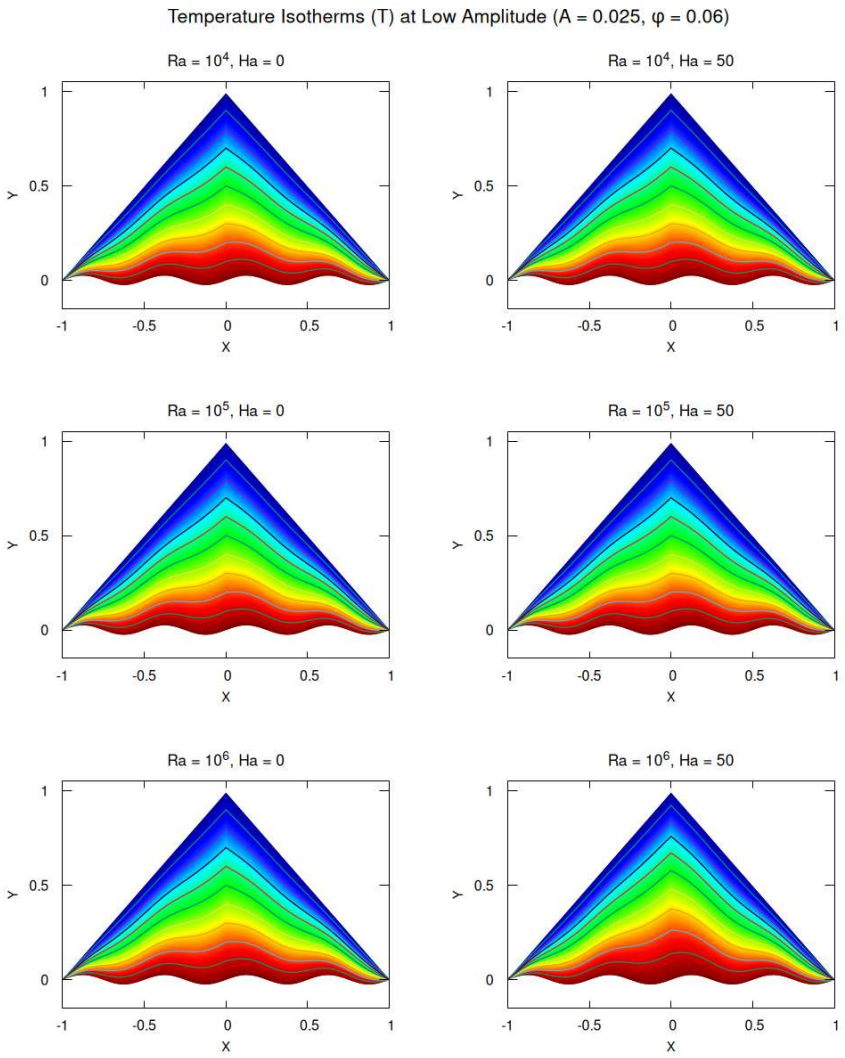


Fig. 15 Isothermal maps at low corrugation amplitude ($A = 0.025, \phi = 0.06$).

Figure 15 illustrates the thermal distributions of $A = 0.025$. At $Ra = 10^4$, linear isotherms confirm a conduction-dominated regime. Increasing buoyancy to $Ra = 10^6$ raises isotherms to a central thermal plume. Activating the magnetic field ($Ha = 50$) suppresses this transport, forcing the profile back to a conduction-dominated state.

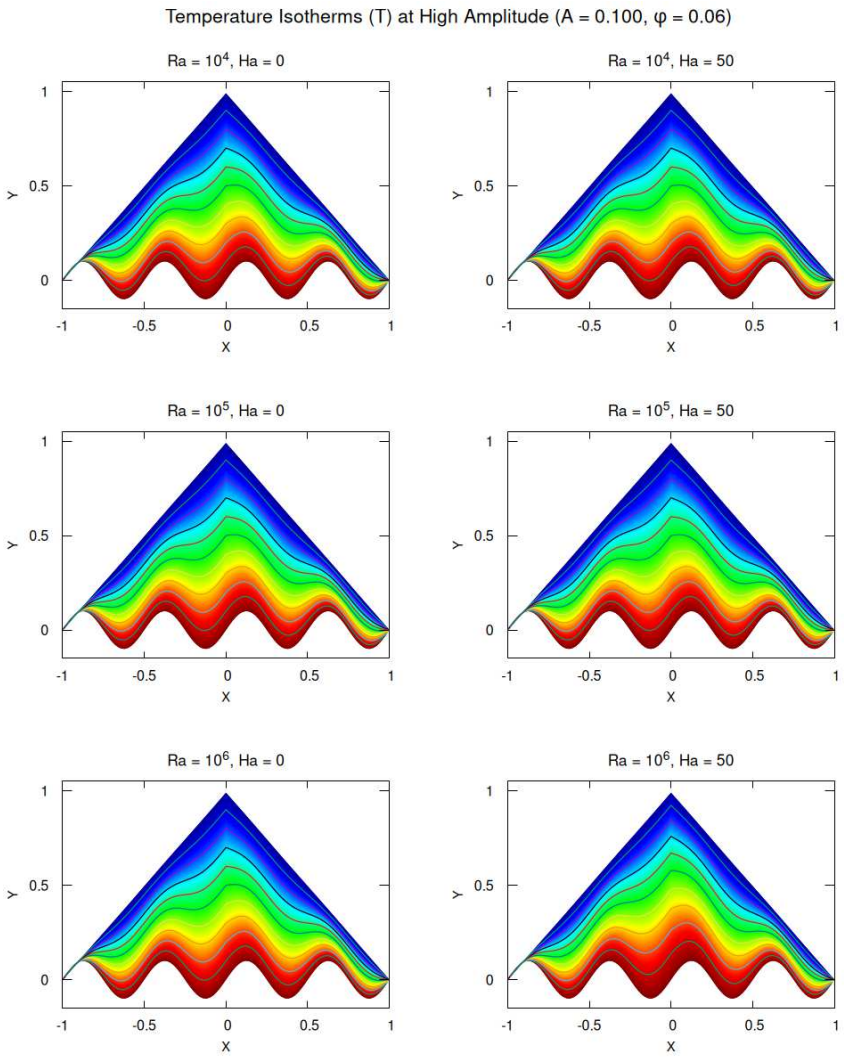


Fig. 16 Isothermal maps at high corrugation amplitude ($A = 0.100, \phi = 0.06$).

Figure 16 presents thermal maps for high amplitude. Geometric restriction is most pronounced here: stagnant nanofluid within deep troughs causes localized thermal compression over wave peaks, significantly altering local heat flux compared to the smoother $A = 0.025$ boundary.

The physical necessity of employing the high-fidelity Khanafer-Vafai model in this specific corrugated configuration is demonstrated by the streamline-isotherm coupling in Figures 13 to 16. Because deep sinusoidal valleys restrict fluid movement, severe local temperature gradients develop within the troughs. Under the Khanafer-Vafai framework, these localized gradients trigger a spatial feedback loop in the effective

dynamic viscosity ($\mu_{nf}(T)$). In the valleys, the heated fluid undergoes a localized drop in viscosity, which slightly accelerates regional recirculation. Traditional constant-property models (such as Maxwell-Brinkman) treat viscosity as spatially uniform, failing to capture these highly localized, temperature-induced shear variations that dictate boundary layer behavior over non-flat walls.

5 Conclusions

A comprehensive numerical investigation of magnetohydrodynamic (MHD) natural convection of a Al_2O_3-water nanofluid inside an isosceles triangular enclosure with a sinusoidal wavy bottom wall was successfully conducted using a Discrete Finite Element Method (DFEM) with an algebraic coordinate transformation. The primary conclusions are summarized as follows:

1. **Grid Transformation Fidelity:** The algebraic non-orthogonal shear mapping correctly aligned the unstructured finite element nodes with the sinusoidal wavy wall ($A\cos(\omega X)$). This transformation eliminated boundary staircase errors and accurately resolved the steep thermal boundary layers without introducing artificial numerical diffusion.
2. **Property Model Sensitivity and Feedback:** Classical analytical models (Maxwell-Brinkman) systematically underestimate the average Nusselt number ($\overline{Nu}$) by up to 7.2% under high-buoyancy states ($Ra = 10^6$) compared to empirical, temperature-dependent correlations (Khanafer-Vafai). This discrepancy arises because the empirical framework captures the localized spatial feedback loop in dynamic viscosity ($\mu_{nf}(T)$); the fluid trapped in deep corrugated valleys undergoes localized heating, reducing local viscosity and accelerating regional micro-recirculation—a phenomenon completely missed by static analytical models.
3. **Active vs. Passive Control Thresholds:** The external magnetic field exerts a strong damping effect on fluid velocity via the horizontal Lorentz force, shifting the primary heat transfer mechanism from active advection to passive conduction. A critical crossover threshold is identified at $Ha \approx 50$, beyond which active electromagnetic braking completely overrides both passive geometric enhancements (A) and nanoparticle-driven advection.
4. **Passive Geometric Control and Conservation:** Increasing the corrugation amplitude (A) enhances local heat transfer by extending the effective surface area and projecting the heated surface into the core fluid stream, yielding an absolute Nusselt increase of $\Delta\overline{Nu} \approx 0.95$ at $Ra = 10^6$. Conversely, the spatial wavelength parameter (λ) has a negligible effect on global thermal performance ($\Delta\overline{Nu} < 0.05$). This indicates a geometric conservation of convective energy, where the added surface area of high-frequency waves is counterbalanced by stagnant, insulating fluid pockets in the narrow valleys.
5. **Multi-Variable Interaction:** While the dispersal of Al_2O_3 nanoparticles increases the dynamic viscosity of the working fluid—introducing additional viscous drag—the accompanying increase in effective thermal conductivity successfully recovers the thermal performance lost to magnetic damping.

The findings of this study provide critical design guidelines for passive-active thermal control in highly restricted geometries, such as attic-shaped enclosures, compact heat exchangers, and solar cavity receivers. The ability to dynamically tune convective heat transfer through the synergistic application of boundary corrugations and electromagnetic field damping, evaluated under a high-fidelity thermophysical framework, offers a highly predictable pathway for optimizing next-generation thermal modules in power-dense environments.

Declarations

Funding

The authors declare that no funds, grants, or other support was received during the preparation of this manuscript.

Competing Interests

The authors have no relevant financial or non-financial interests to disclose.

Data Availability

The datasets generated and/or analyzed during the current study are available from the corresponding author on reasonable request.

References

[1] H. F. Oztop and E. Abu-Nada. Numerical study of natural convection in partially heated rectangular enclosures filled with nanofluids. *International Journal of Heat and Fluid Flow*, 29:1326–1336, 2008. doi: 10.1016/j.ijheatfluidflow.2008.04.009.

[2] K. Khanafer, K. Vafai, and M. Lightstone. Buoyancy-driven heat transfer enhancement in a two-dimensional enclosure utilizing nanofluids. *International Journal of Heat and Mass Transfer*, 46:3639–3653, 2003. doi: 10.1016/S0017-9310(03)00156-X.

[3] B. Ghasemi, S. M. Aminossadati, and A. Raisi. Magnetic field effect on natural convection in a nanofluid-filled square enclosure. *International Journal of Thermal Sciences*, 50:1748–1756, 2011. doi: 10.1016/j.ijthermalsci.2011.04.010.

[4] M. Sheikholeslami, M. Gorji-Bandpy, and D. D. Ganji. Natural convection heat transfer in a cavity with sinusoidal wall filled with cuo–water nanofluid in presence of magnetic field. *Journal of the Taiwan Institute of Chemical Engineers*, 45:40–49, 2014. doi: 10.1016/j.jtice.2013.04.019.

[5] A. S. Dogonchi, M. Alizadeh, and D. D. Ganji. Investigation of mhd natural convection of al2o3-water nanofluid in a wavy cavity using cvfem. *Journal of Molecular Liquids*, 233:441–452, 2017. doi: 10.1016/j.molliq.2017.03.041.

[6] F. Selimefendigil and H. F. Oztop. Mhd natural convection and entropy generation of nanofluid in a cavity with wavy walls. *International Journal of Mechanical Sciences*, 145:312–325, 2018. doi: 10.1016/j.ijmecsci.2018.07.021.

[7] N. S. Bondareva and M. A. Sheremet. Mhd natural convection in a wavy cavity filled with a nanofluid under the effects of brownian motion. *International Journal of Heat and Mass Transfer*, 103:943–955, 2016. doi: 10.1016/j.ijheatmasstransfer.2016.08.014.

[8] M. M. Rahman, H. F. Oztop, and R. Saidur. Augmentation of natural convection heat transfer in triangular shape solar collector by utilizing water based nanofluids having a corrugated bottom wall. *International Communications in Heat and Mass Transfer*, 50:117–127, 2014. doi: 10.1016/j.icheatmasstransfer.2013.10.008.

[9] M. A. Sheremet and I. Pop. Natural convection in a wavy porous cavity filled with a nanofluid using buongiorno's mathematical model. *International Journal of Heat and Mass Transfer*, 82:75–85, 2015. doi: 10.1016/j.ijheatmasstransfer.2014.11.026.

[10] A. I. Alsabery, A. J. Chamkha, and I. Hashim. Natural convection flow and heat transfer in a wavy cavity filled with a nanofluid using variable properties. *International Journal of Mechanical Sciences*, 131:701–716, 2017. doi: 10.1016/j.ijmecsci.2017.08.025.

[11] M. A. Mansour and S. E. Ahmed. Mhd natural convection in a triangular cavity filled with a nanofluid: Effects of localized heating. *Journal of Magnetism and Magnetic Materials*, 419:143–151, 2016. doi: 10.1016/j.jmmm.2016.06.012.

[12] D. Tripathi and O. A. Bég. A study on magnetohydrodynamic nanofluid transport in corrugated channels with thermal radiation. *Journal of Molecular Liquids*, 222:310–320, 2016. doi: 10.1016/j.molliq.2016.07.033.

[13] S. Saha, C. Lei, and J. Patterson. Natural convection in a triangular enclosure subject to periodic thermal forcing. In *Proceedings of the 13th International Heat Transfer Conference*, 2006. doi: 10.1615/IHTC13.p6.430.

[14] H. C. Brinkman. The viscosity of concentrated suspensions and solutions. *The Journal of Chemical Physics*, 20:571–581, 1952. doi: 10.1063/1.1700493.

[15] J. C. Maxwell. *A Treatise on Electricity and Magnetism*. Clarendon Press, Oxford, 1873.

[16] B. Ghasemi and S. M. Aminossadati. Mixed convection heat transfer in a lid-driven triangular enclosure filled with nanofluid. *International Communications in Heat and Mass Transfer*, 36:1166–1172, 2009. doi: 10.1016/j.icheatmasstransfer.2009.08.006.

[17] S. Hussain, S. E. Ahmed, and T. Akbar. Entropy generation and mhd natural convection in an inclined triangular enclosure utilizing copper-water nanofluid mixtures. *International Communications in Heat and Mass Transfer*, 116:104670, 2020. doi: 10.1016/j.icheatmasstransfer.2020.104670.

[18] B. Mliki, M. A. Abbassi, and A. Omri. Augmentation of natural convection in an asymmetric triangular cavity using multi-walled carbon nanotubes. *Journal of Molecular Liquids*, 250:115–128, 2018. doi: 10.1016/j.molliq.2017.11.135.

[19] A. A. Avramenko, D. G. Blinov, and I. V. Shevchuk. Self-similar analysis of nanofluid natural convection over a corrugated vertical boundary surface. *International Journal of Heat and Mass Transfer*, 93:290–299, 2016. doi: 10.1016/j.ijheatmasstransfer.2015.09.091.

[20] R. K. Tiwari and M. K. Das. Heat transfer augmentation in a two-sided lid-driven differentially heated square cavity utilizing nanofluids. *International Journal of Heat and Mass Transfer*, 50:2002–2018, 2007. doi: 10.1016/j.ijheatmasstransfer.2006.10.034.

[21] M. Sheikholeslami and D. D. Ganji. Nanofluid flow and heat transfer in a semi-annulus enclosure under the effect of magnetic field. *Journal of Molecular Liquids*, 195:54–61, 2014. doi: 10.1016/j.molliq.2014.02.015.

[22] F. Garoosi and B. Rohani. Numerical simulation of natural convection of nanofluid in a cavity with several corrugated heating blocks. *Journal of Molecular Liquids*, 224:1300–1315, 2016. doi: 10.1016/j.molliq.2016.10.105.

[23] J. Buongiorno. Convective transport in nanofluids. *Journal of Heat Transfer*, 128:240–250, 2006. doi: 10.1115/1.2150834.

[24] S. U. S. Choi. Enhancing thermal conductivity of fluids with nanoparticles. In *ASME International Mechanical Engineering Congress and Exposition*, 1995. doi: 10.1115/IMECE1995-0926.

[25] E. Abu-Nada, Z. Masoud, and H. F. Oztop. Effect of nanofluid variable properties on natural convection in enclosures. *International Journal of Thermal Sciences*, 49:479–491, 2010. doi: 10.1016/j.ijthermalsci.2009.09.002.

[26] M. A. Sheremet and I. Pop. Natural convection in a triangular cavity filled with a nanofluid with localized heating. *International Journal of Heat and Mass Transfer*, 121:75–84, 2018. doi: 10.1016/j.ijheatmasstransfer.2018.01.002.

[27] K. Khanafer and K. Vafai. A critical synthesis of thermophysical characteristics of nanofluids. *International Journal of Heat and Mass Transfer*, 54:4410–4428, 2011. doi: 10.1016/j.ijheatmasstransfer.2011.04.048.

[28] H. E. Patel, T. Sundararajan, and S. K. Das. An experimental investigation into the thermal conductivity enhancement and viscosity of stable and aqueous al2o3 nanofluids. *Journal of Nanoparticle Research*, 12:1015–1027, 2010. doi: 10.1007/s11051-009-9653-y.

[29] C. J. Ho, M. W. Chen, and Z. W. Li. Numerical simulation of natural convection of nanofluid in a square enclosure. *International Journal of Thermal Sciences*, 47:1346–1353, 2008. doi: 10.1016/j.ijthermalsci.2007.12.001.

[30] H. Asan and L. Namli. Laminar natural convection in a pitched roof of triangular cross-section. *International Communications in Heat and Mass Transfer*, 27: 253–262, 2000. doi: 10.1016/S0735-1933(00)00107-1.

[31] E. F. Kent. Numerical analysis of laminar natural convection in isosceles triangular enclosures for cold base and hot inclined walls. *Mechanics Research Communications*, 36:497–508, 2009. doi: 10.1016/j.mechrescom.2008.11.002.

[32] T. Basak, S. Roy, and S. K. Singh. Finite element analysis of natural convection in a triangular cavity with various thermal boundary layouts. *International Journal of Heat and Mass Transfer*, 53:1419–1433, 2010. doi: 10.1016/j.ijheatmasstransfer.2009.11.023.

[33] B. Ghasemi and S. M. Aminossadati. Natural convection in a nanofluid-filled triangular enclosure divided by a solid partition. *International Communications in Heat and Mass Transfer*, 37:1133–1139, 2010. doi: 10.1016/j.icheatmasstransfer.2010.06.002.

[34] M. M. Hasan and S. C. Saha. Numerical study of natural convection in a triangular enclosure with a wavy vertical wall. *International Journal of Thermal Sciences*, 109:148–158, 2016. doi: 10.1016/j.ijthermalsci.2016.06.007.

[35] A. Mahmoudi, I. Pop, and M. Shahi. Effect of magnetic field on natural convection in a triangular cavity utilizing nanofluid and equipped with a wavy wall. *Journal of Magnetism and Magnetic Materials*, 343:111–122, 2013. doi: 10.1016/j.jmmm.2013.04.062.

[36] M. M. Rahman, H. F. Öztop, A. Ahsan, M. A. Kalam, and Y. Varol. Double-diffusive natural convection in a triangular solar collector. *International Communications in Heat and Mass Transfer*, 39:257–265, 2012. doi: 10.1016/j.icheatmasstransfer.2011.12.003.

[37] F. Selimefendigil and H. F. Öztop. Mhd mixed convection of nanofluid filled partially heated triangular enclosure with a rotating adiabatic cylinder. *Journal of the Taiwan Institute of Chemical Engineers*, 45:2150–2162, 2014. doi: 10.1016/j.jtice.2014.06.018.

[38] S. C. Saha. Natural convection heat transfer in a baffled triangular enclosure. *Proceedings of the 15th International Heat Transfer Conference*, 2014. doi: 10.1615/IHTC15.nat.007626.

[39] M. Shekaramiz, S. Fathi, H. A. Ataabadi, and D. Toghraie. Mhd nanofluid free convection inside the wavy triangular cavity considering periodic temperature boundary condition and velocity slip mechanisms. *International Journal of Thermal Sciences*, 170:107179, 2021. doi: 10.1016/j.ijthermalsci.2021.107179.

[40] F. Garoosi, M. Mollazadeh, and F. Talebi. Natural convection of nanofluids in different enclosures: A review. *Journal of Molecular Liquids*, 215:413–431, 2016. doi: 10.1016/j.molliq.2016.01.077.

[41] R. Nasrin and M. A. Alim. Numerical study of natural convection in a triangular cavity with an internal heat generating element. *International Journal of Heat and Mass Transfer*, 52:5259–5267, 2009. doi: 10.1016/j.ijheatmasstransfer.2009.06.018.

[42] S. Singh and R. Bhargava. Numerical study of natural convection within a wavy enclosure using meshfree approach: Effect of corner heating. *The Scientific World Journal*, 2014:842401, 2014. doi: 10.1155/2014/842401.

[43] A. S. Dogonchi, M. Hashemi-Tilehnoee, and D. D. Ganji. Mhd natural convection of a nanofluid in a triangular enclosure with a wavy base under variable thermal boundary constraints. *Advanced Powder Technology*, 30:943–956, 2019. doi: 10.1016/j.apt.2019.02.008.

[44] P. A. Davidson. *An Introduction to Magnetohydrodynamics*. Cambridge University Press, 2001. doi: 10.1017/CBO9780511626333.

[45] K. M. Khanafer and A. J. Chamkha. Hydromagnetic natural convection from an inclined porous square enclosure with heat generation. *Numerical Heat Transfer, Part A: Applications*, 33:891–910, 1998. doi: 10.1080/10407789808913972.

[46] A. J. Chamkha. Hydromagnetic natural convection from an inclined heated plate in a non-darcy porous medium. *International Journal of Heat and Mass Transfer*, 40:4217–4228, 1997. doi: 10.1016/S0017-9310(97)00034-7.

[47] B. Ghasemi and S. M. Aminossadati. Mhd natural convection in a nanofluid-filled enclosure. *International Journal of Thermal Sciences*, 49:2138–2146, 2010. doi: 10.1016/j.ijthermalsci.2010.06.002.

[48] R. Moreau. *Magnetohydrodynamics*. Kluwer Academic Publishers, 1990. doi: 10.1007/978-94-015-7883-7.

[49] J. P. Garandet, T. Alboussiere, and R. Moreau. Buoyancy driven convection in a rectangular cavity with a horizontal magnetic field. *International Journal of Heat and Mass Transfer*, 35:741–748, 1992. doi: 10.1016/0017-9310(92)90111-H.

[50] F. Selimefendigil and H. F. Oztop. Mhd mixed convection in a nanofluid filled cavity with a wavy wall and an inner rotating cylinder. *International Journal of Mechanical Sciences*, 114:123–140, 2016. doi: 10.1016/j.ijmecsci.2016.05.014.

[51] A. S. Dogonchi, M. Alizadeh, and A. J. Chamkha. Mhd natural convection and entropy generation of al2o3-water nanofluid in a triangular cavity with a wavy boundary profile. *Journal of Thermal Analysis and Calorimetry*, 139:603–619, 2020. doi: 10.1007/s10973-019-08390-y.

[52] J. F. Thompson, Z. U. A. Warsi, and C. W. Mastin. Boundary-fitted coordinate systems for numerical solution of partial differential equations: A review. *Journal of Computational Physics*, 47:1–108, 1982. doi: 10.1016/0021-9991(82)90117-6.

[53] Y. U. U. B. Turabi, S. Ahmad, S. Munir, T. Muhammad, A. S. Alshomrani, and M. A. H. Al-Hamami. Natural convective flow of hybrid nanofluid in a triangular enclosure with heated wavy wall and cold obstacle. *Case Studies in Thermal Engineering*, 73:106515, 2025. doi: 10.1016/j.csite.2025.106515.

[54] S. Soleimani, M. Sheikholeslami, and D. D. Ganji. Natural convection of nanofluid in a semi-annulus enclosure with the presence of magnetic field. *International Communications in Heat and Mass Transfer*, 39:558–564, 2012. doi: 10.1016/j.icheatmasstransfer.2012.02.009.

[55] L. A. A. Mahdi, H. A. A. Wahhab, and M. T. Chaichan. Entropy generation analysis for vertical flat and corrugated surface by natural convection and radiation at constant heat flux. *Case Studies in Thermal Engineering*, 61:104979, 2024. doi: 10.1016/j.csite.2024.104979.